Research Article | Vol. 16, No. 10 / 1 Oct 2025 / Biomedical Optics Express 4003
Biomedical Optics EXPRESS

Evaluation of radio frequency ablation in human left atrial tissues for atrial fibrillation using optical coherence tomography

EBENEZER RAJ SELVARAJ MERCYSHALINIE,[1] DYLAN O. PATTERSON,[2] BORNFACE M. MUTEMBEI,[1] AVERY D. LADYMON,[3] FENG YAN,[1] KAUSTUBH PANDIT,[3] HAYDEN PEEK,[1] KAR-MING A. FUNG,[4] QINGHAO ZHANG,[1] CHEN WANG,[1] YAN CUI,[1] JUNYUAN LIU,[1] RONGHAO LIU,[1] PAULO MARTINS,[5] STAVROS STAVRAKIS,[6] KE ZHANG,[1,7] DAVID R. MILLER,[1,8] AND QINGGONG TANG[1,9]

[1]*Peggy and Charles Stephenson School of Biomedical Engineering, University of Oklahoma, Norman, OK, 73019, USA*
[2]*School of Biological Sciences, University of Oklahoma, Norman, OK, 73071, USA*
[3]*Aerospace and Mechanical Engineering, University of Oklahoma, Norman, OK, 73071, USA*
[4]*Department of Pathology, University of Oklahoma Health Sciences Center, Oklahoma City, OK, 73117, USA*
[5]*Department of Surgery, Transplant Institute, University of Oklahoma Health Sciences Center, Oklahoma City, OK, 73117, USA*
[6]*Department of Internal Medicine, University of Oklahoma Health Science Center, Oklahoma City, OK, 73117, USA*
[7]*kezhang@ou.edu*
[8]*dmiller@ou.edu*
[9]*qtang@ou.edu*

Abstract: Despite its widespread adoption, the success of radiofrequency (RF) ablation is often limited by challenges in achieving durable, transmural lesions while avoiding complications such as incomplete ablation or over-ablation. Optical coherence tomography (OCT) offers high-resolution visualization of cardiac tissue, enabling real-time assessment of lesion depth. Therefore, we investigated the impact of RF ablation on donated human left atrial tissue using an OCT imaging system to assess lesion formation in a controlled laboratory setting. RF ablation lesions were created at durations of 20, 40, 60, 80, and 100 seconds (s), and their effects were quantified by calculating the attenuation coefficient from OCT images. To identify tissue regions in the image, a U-Net model was employed for segmentation, achieving a mean intersection over union (IoU) of 0.9748 with an inference time of 82 milliseconds. Our results demonstrated clear differences in tissue response before and after ablation, with distinct lesion characteristics across the tested durations. One-way ANOVA analysis yielded a p-value of 1.09×10^{-8}, confirming statistically significant differences among the ablation durations. These findings highlight the potential of SD-OCT for precise, real-time monitoring of ablation effects. Future work aims to integrate OCT with ablation catheters for clinical applications, enhancing the precision of catheter-based treatments for conditions like atrial fibrillation.

1. Introduction

Atrial fibrillation (AF) remains one of the most prevalent cardiac arrhythmias, affecting millions globally and posing significant risks of stroke, heart failure, and mortality [1,2]. Radiofrequency (RF) catheter ablation has emerged as a cornerstone therapy for AF, particularly through pulmonary

#570328 https://doi.org/10.1364/BOE.570328
Journal © 2025 Received 12 Jun 2025; revised 1 Aug 2025; accepted 26 Aug 2025; published 10 Sep 2025

Biomedical Optics EXPRESS

vein isolation (PVI) in the left atrium (LA), which targets ectopic triggers and modifies the atrial substrate to restore sinus rhythm [3,4]. Although widely adopted, the effectiveness of RF ablation is often constrained by difficulties in creating durable, transmural lesions without causing complications such as incomplete or excessive ablation, which can lead to tissue damage, pulmonary vein stenosis, or esophageal injury [5,6]. Clinically, ablation times typically hover around 30 seconds per lesion, but optimal durations remain poorly defined, particularly when balancing efficacy against the risks of excessive energy delivery [7,8]. Understanding the precise effects of ablation duration on LA tissue is critical for improving procedural outcomes and guiding clinicians in tailoring treatment for AF patients.

The left atrium's complex anatomy and variable tissue characteristics necessitate precise monitoring of ablation effects to ensure lesion quality and procedural safety [9,10]. Traditional electrophysiological measurements, such as electrical isolation, provide limited insight into the structural and microstructural changes induced by ablation [11]. Advanced imaging modalities, such as spectral-domain optical coherence tomography (SD-OCT), offer high-resolution visualization of cardiac tissue, enabling real-time assessment of lesion depth and transmurality [12,13]. The attenuation coefficient, derived from SD-OCT images, is a particularly sensitive metric for detecting subtle tissue alterations, making it an ideal tool for quantifying ablation-induced changes [14,15]. However, SD-OCT images are often plagued by noise, which can obscure critical details. Deep learning models, such as the U-Net architecture, have shown remarkable efficacy in segmenting medical images, enhancing the accuracy of quantitative analyses like calculating the attenuation coefficient [16,17].

In this study, we investigate the impact of varying RF ablation durations (20, 40, 60, 80, and 100 seconds) on human left atrial tissue, using a controlled *ex vivo* setup where the LA is maintained to mimic physiological conditions. Ablation was performed perpendicularly at 30 Watts and 60° C, reflecting standard clinical parameters, with extended durations to explore the effects of over-ablation. Pre- and post-ablation SD-OCT imaging was employed to capture tissue changes, with a U-Net model applied to segment images and facilitate precise calculation of the attenuation coefficient. This approach allows us to quantify microstructural changes in the LA and correlate them with ablation time, providing insights into optimal durations for clinical practice. By addressing the gap in understanding how ablation duration influences tissue response, this work aims to enhance the precision of RF ablation for AF, ultimately improving patient outcomes and reducing procedural risks.

The motivation for this study stems from the need to optimize ablation strategies in the context of AF's growing prevalence and the limitations of current techniques [18,19]. Prior studies, primarily conducted on animal models, have highlighted the importance of lesion transmurality for preventing AF recurrence but have rarely explored the effects of prolonged ablation times or leveraged advanced imaging to assess tissue changes quantitatively [20,21]. Our use of SD-OCT and U-Net-based segmentation builds on recent advancements in cardiac imaging and machine learning, offering a novel framework for evaluating ablation effects [22,23]. This research also aligns with ongoing efforts to refine ablation technologies, such as contact force-sensing catheters and real-time lesion monitoring, which aim to standardize and improve procedural outcomes [24,25]. By systematically analyzing the interplay between ablation duration, tissue response, and imaging-based metrics, we seek to provide actionable data for clinicians and contribute to the evolving landscape of AF management [26,27].

2. Materials and methods

2.1. SD OCT system and imaging configuration

In this study, imaging was conducted using a Thorlabs Telesto Series Spectral-Domain Optical Coherence Tomography (SD-OCT) system (TEL321C1), operating at a 1300 nm center wavelength with a 5.5 μm axial resolution and a 3.5 mm imaging depth in air, enabling high-resolution

Biomedical Optics EXPRESS

visualization of microstructural changes in the left atrium before and after ablation. The system is equipped with an OCTG13 standard scanner and OCT-LK3 scan lens kit, offering a 10 mm x 10 mm field of view and 13 µm lateral resolution. A schematic diagram of the SD-OCT system is presented in Fig. 1. The emitted laser from the light source is split into two paths for reference and sample arms, respectively. In the reference path, the beam is directed through an achromatic lens and reflected by a mirror, forming the reference signal. Concurrently, in the sample arm, the beam is scanned by a galvanometer scanner and focused on the tissue using an achromatic lens. The back-reflected signals from both arms are recombined at the coupler, producing interference patterns that are delivered to a spectrometer equipped with a diffraction grating for spectral decomposition and subsequent signal analysis. The ThorImage OCT software was used to acquire and process 3D datasets. The imaging parameters were configured as 9 mm (X) x 9 mm (Y) x 2.6 mm (Z), with a pixel size of 5 µm (X) x 20 µm (Y) x 2.54 µm (Z), and a 48 kHz A-line rate.

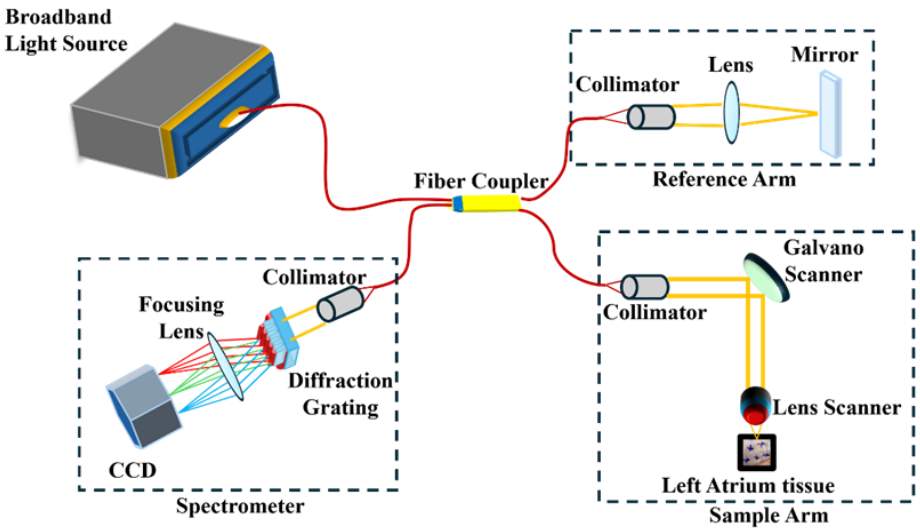

Fig. 1. Schematic diagram of the SD-OCT system configuration.

2.2. *Experimental setup for ablating the left atrium*

This study was approved by the University of Oklahoma and the University of Oklahoma Health Sciences Center Institutional Review Board (IRB) (Study number: IRB #12462). All the experiment-used human heart samples were preserved by cold preservation solution (University of Wisconsin solution) for keeping the heart sample's physiological status and imaged within 2 days after removing from the donors. Five human hearts were used in the study and none of the donors suffered from heart attack as the cause of death or no significant history of heart disease. The experimental setup for this RF ablation study on the *ex vivo* human left atrial tissue was designed to simulate clinical conditions and enable precise imaging of ablation-induced changes using the SD-OCT system. The setup, illustrated in Fig. 2, facilitated controlled ablation at varying durations and high-resolution imaging to quantify tissue alterations, with a focus on optimizing ablation parameters for atrial fibrillation treatment. The following describes tissue preparation, ablation, and imaging procedures, emphasizing reproducibility and accuracy.

2.2.1. Tissue preparation and wet bath configuration

Five fresh human hearts were used for the experiments (Fig. 2(a)). The left and right atria and an incision was made along the atrial septum to separate them. The left atrium, characterized by

Biomedical Optics EXPRESS

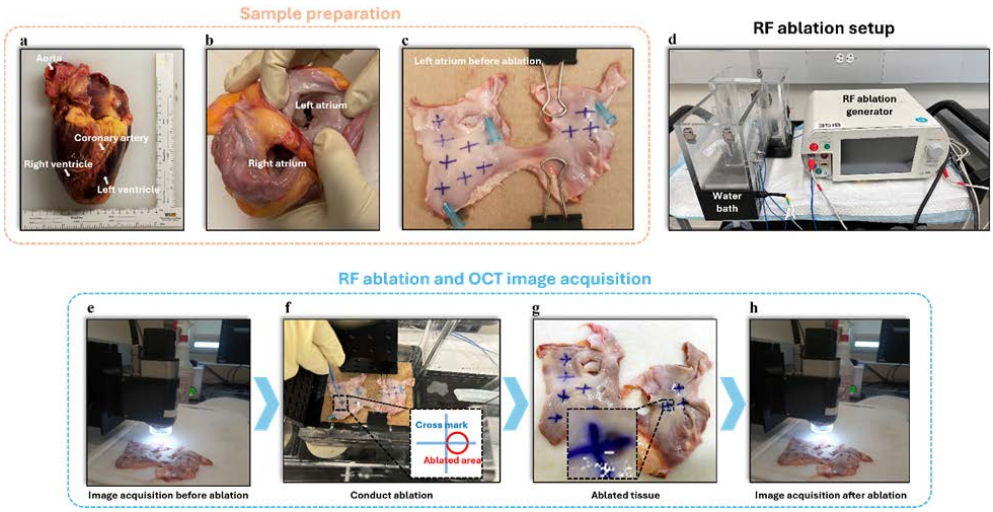

Fig. 2. Schematic illustration of the experimental setup and workflow.

its smooth endocardial surface, was isolated for ablation, in contrast to the veiny right atrium with prominent pectinate muscles (Fig. 2(b)). The isolated left atrium was pinned flat onto a cardboard base using metal clips (Fig. 2(c)). All ablations were performed within 1 hour of dissection to maintain tissue viability.

A wet bath was prepared in a lab cart (Fig. 2(d)). The bath was filled to three-quarters capacity with room-temperature 0.9% saline solution, consistent with prior studies demonstrating enhanced lesion formation in saline-enhanced RF ablation [28]. The solution was stirred to ensure uniform salinity. The stabilized left atrium was then submerged in the saline bath for ablation ensuring consistent electrical conductivity and tissue hydration.

2.2.2. RF ablation procedure

The RF ablation was performed utilizing a SmartAblater generator (Biosense Webster) set to 30 Watts, with the catheter tip ($d = 2$ mm) temperature controlled at 60° C to reflect standard clinical practice (Fig. 2(d)). The catheter was connected to the generator and calibrated prior to use. Multiple ablation spots were marked on the flattened left atrium using a sterile surgical skin marker (TONDAUS, 0.5 mm and 1.0 mm tips) (Fig. 2(c)). Each spot was subjected to a single ablation with a specific duration—either 20, 40, 60, 80, or 100 seconds—to systematically investigate the effect of varying ablation times. During each ablation, the catheter tip was positioned perpendicularly to the tissue to ensure consistent energy delivery (Fig. 2(f)). This standardized setup enabled reliable comparisons across different ablation durations. Visible lesions were observed on the tissue surface (Fig. 2(g)), confirming successful energy application. Prior to ablation, 3D OCT images of all marked spots were acquired to establish baseline tissue characteristics (Fig. 2(e)). Following ablation, 3D OCT imaging was repeated at each site to document lesion features (Fig. 2(h)).

2.2.3. Histological validation of ablation lesions

After imaging, the ablated left atrial samples were excised and preserved in 10% neutral buffered formalin solution in histology jars for subsequent histopathological analysis. Reticulin and Trichome staining were performed to evaluate tissue morphology, validate ablation-induced changes, and provide additional insight into the histopathological effects of RF energy on atrial tissue. Reticulin staining is a histological technique used to visualize reticulin fibers, which

Biomedical Optics EXPRESS

are delicate connective tissue fibers composed primarily of type III collagen. On the other hand, Trichrome staining was used to distinguish collagen from muscle. This staining method highlights the structural framework of tissues and aids in morphological assessment [29].

2.3. Tissue region segmentation in OCT images

The original left atrium images obtained via OCT consistently contain an empty space above the tissue (see Fig. 3(a)), which could interfere with subsequent image processing. To isolate tissue regions in OCT cross-sectional images, a deep learning-based segmentation step was implemented. This approach aimed at excluding the non-tissue region above the sample, retaining only the tissue section for further quantitative analysis. Five deep learning models— U-Net [16], Pix2Pix [30], SAM-2-Unet [31], ResNet50 [32] and nnU-Net [33]—were evaluated for their ability to accurately segment tissue regions. The U-Net architecture, proposed by Ronneberger et al. [16], features an encoder-decoder structure with skip connections and is widely recognized for its strong segmentation performance, even when training data is limited. Pix2Pix, a conditional generative adversarial network (CGAN) described by Isola et al. [30], consists of a U-Net-based generator and a PatchGAN discriminator, making it well-suited for image-to-image translation tasks. SAM (Segment Anything Model) is a transformer-based deep learning model for image segmentation. It utilizes a vision transformer (ViT) backbone with promptable segmentation heads to generate high-quality masks for objects within the image. Trained on a massive dataset of 1 billion masks, SAM is capable of zero-shot generalization to unseen images. Here, we finetuned the SAM2-UNet model, a variant of the SAM, which leverages the powerful, hierarchically pre-trained SAM 2 encoder with a U-Net decoder. SAM2-UNet is more suitable for medical images

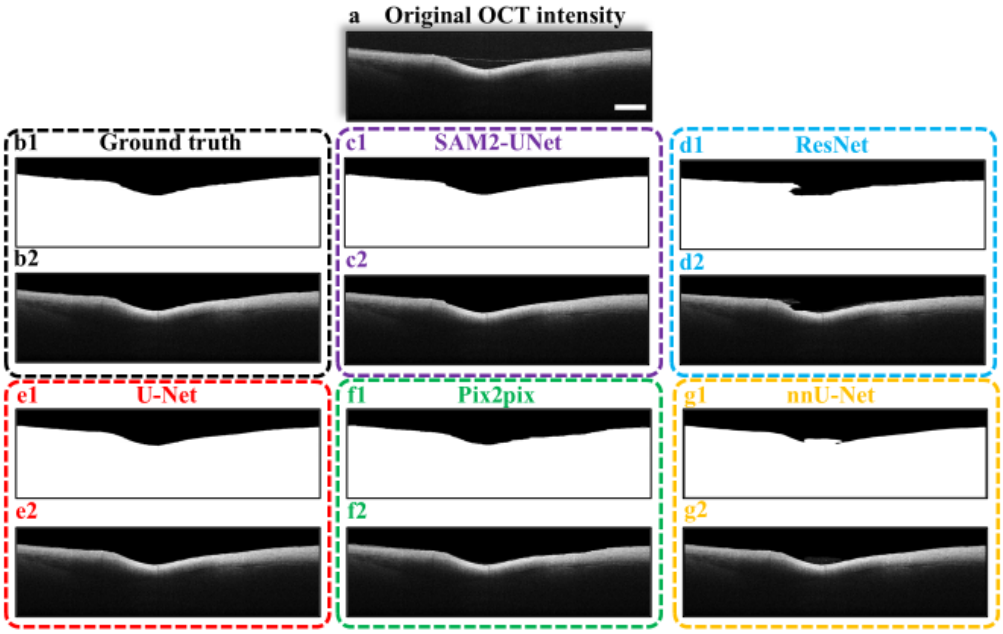

Fig. 3. Evaluation of SAM2-UNet, ResNet, U-Net, Pix2Pix and nnU-Net version 2 models for mask prediction performance on SD-OCT intensity images. (a) Original OCT intensity image. (b1) Ground truth mask; (b2) Masked original intensity image using ground truth. (c1-g1) Predicted masks, and (c2-g2) corresponding masked images produced by SAM2-UNet, ResNet, U-Net, Pix2Pix and nnU-Net version 2 respectively. All models are assessed for their capability to segment left atrial tissues. Scale bar: 900 μm.

Biomedical Optics EXPRESS

as its hierarchical Hiera backbone, unlike plain ViT encoders, excels at capturing multiscale features [31]. This, combined with its classic U-Net decoder, enables precise, task-specific, and class-specific segmentation, overcoming the class-agnostic limitations of standalone SAM 2 for medical domains [31,34]. ResNet50 is a 50-layer deep convolutional neural network from the Residual Network family, featuring skip connections to mitigate vanishing gradients and using 3×3 convolutions and bottleneck blocks for efficient feature extraction. Lastly, the no-new-net (nnU-Net) is a robust and self-adapting framework for U-Net-based medical image segmentation. It automatically configures and optimizes all aspects of the segmentation pipeline, including preprocessing, network architecture (2D, 3D, or cascaded U-Nets), training, and inference. This ability to adapt to a dataset enabled nnU-Net to outperform other state-of-the-art segmentation models in the Medical Segmentation Decathlon challenge [33]. A total of 6057 manually labeled liver OCT images [35] were used for training (80%), validation (10%), and testing (10%) in the task of liver tissue segmentation. All computational experiments were performed using Python (Python Org, version 3.12.8) on a workstation running Windows 10 with 32.0 GB of physical memory equipped with a NVIDIA 4090 graphical processing unit.

Post-training, each model was further tested on a set of 600 post-ablation heart OCT images, for which the corresponding masks were manually segmented to serve as ground truth. Table 1 lists the hyperparameters used to train the five models. After applying the best model to generate binary masks, we first filled the holes in the image, followed by a median filtering (kernel = 3) to smoothen the edges. In the final step, we applied the binary masks to the OCT images to segment the region of interest from the background. This process was not aimed at typical speckle noise reduction within the tissue but was exclusively for isolating the tissue signal to ensure accurate attenuation coefficient calculations. Importantly, no alterations were performed on the pixel values within the tissue region itself, preserving the integrity of the original data.

Table 1. Hyperparameters used to train deep learning models for tissue segmentation. U-Net, Pix2pix, Segment Anything-2 model with U-Net, ResNet-50 and no-new-U-Net model

Hyperparameter	U-net	Pix2pix	SAM2-U-Net	ResNet-50	nnU-Net v2
Learning rate	5e-4	5e-4	1e-2	5e-4	1e-2
β	0.5	0.5	1e-7	0.5	NA
# iterations	NA	NA	250	NA	250
# epochs	40000	40000	1000	40000	1000
Batch size	1	1	4	1	Self-configured
Optimizer	Adam	Adam	Adam	Adam	Self-configured
Weight decay	NA	NA	3e-5	NA	3e-5, linear

2.4. *Attenuation coefficient quantification of ablation effects based on the Beer–Lambert law*

To quantitatively evaluate the impact of RF ablation on human left atrial tissue, attenuation coefficients (μ) were derived from SD-OCT images based on the Beer-Lambert law [36]:

$$\ln I(z) = \ln(I_0) - \mu z$$

where I(z) is the OCT signal intensity at depth Z, and I_0 is the initial intensity. These coefficients serve as sensitive markers of structural alterations in tissue induced by thermal damage, reflecting changes in optical scattering and absorption. Attenuation coefficients were calculated along each column of OCT cross-sectional images, starting from the tissue surface identified by the U-Net segmentation and extending downward for 150 pixels (~380 μm), encompassing the visible tissue region.

Biomedical Optics EXPRESS

3. Results

3.1. Performance comparison of segmentation models

Model performance was evaluated using seven metrics to provide a comprehensive assessment. In addition to balanced accuracy, recall, precision, and mean IoU [16], we incorporated the average Hausdorff distance (AHD) and volumetric similarity (VS). The AHD quantifies boundary alignment by measuring how closely the points of the segmented mask lie to the ground truth, with lower values indicating a better match [37,38]. VS provides a volume-based similarity score between the segmentation and ground truth [38]. Finally, given its importance for clinical applicability, we compared the inference time required to process 600 images. As summarized in Table 2, the U-Net model delivered the best overall balance of accuracy, efficiency, and reliability. While other models like SAM2-UNet achieved high scores in certain metrics, U-Net achieved the highest VS value (0.9938) and a highly competitive mean IoU of 0.9748. Crucially, U-Net was the most computationally efficient, achieving the fastest inference time of 49.375 s (82 milliseconds per image), outperforming Pix2pix (49.812 s) and SAM2-UNet (79.530 s). Figure 3 visually confirms that U-Net accurately delineates the boundary between tissue and the overlying air region. This exceptional combination of high accuracy, compact size, and superior processing speed confirms its robustness and supports its use in subsequent analyses, underlining its clinical deployment potential.

Table 2. Comparison of the segmentation performance of SAM2-UNet, ResNet, U-Net, Pix2pix and nnU-Net version 2 on the SD-OCT intensity images

Models	Balanced Accuracy	Recall	Precision	Mean IoU	Average Hausdorff Distance (pixels)	Volumetric Similarity	Inference time (n = 600)	Model size in parameters (10^6)
SAM2-UNet	0.9898	0.983	0.9982	0.9812	12.0577	0.9921	79.530 s	≥241.4 [39]
ResNet	0.9441	0.9024	0.991	0.8942	35.1826	0.9418	146.542s	68.29
U-Net	0.9820	0.9904	0.9842	0.9748	15.5719	0.9938	49.375s	54.43
Pix2pix	0.9796	0.986	0.9824	0.9687	17.2573	0.9913	49.812s	57.20
nnU-Net	0.9789	0.9931	0.975	0.9726	17.5308	0.9864	61.9460s	33.47

3.2. Attenuation coefficient trends over ablation time

Figure 4 illustrates the structural and optical property changes in human left atrium tissue captured by SD-OCT before and after RF ablation over increasing time intervals. Prior to ablation, the tissue surface appears generally smooth, and the attenuation coefficient map shows no signs of ablation-related changes. After 20 s of RF ablation, the tissue intensity image and 3D view do not exhibit noticeable changes; however, the corresponding attenuation coefficient map reveals a distinct circular region, indicative of thermal damage, collagen denaturation, and cellular disruption caused by ablation. From 40 to 100 s, ablation effects become more evident, with clear surface indentations observed in both the intensity images and 3D views, as well as corresponding changes in the attenuation coefficient maps.

This approach provided a quantitative and visual assessment of tissue response to ablation, offering insights into the depth of thermal injury and tissue homogeneity alterations. The method's ability to map spatial variations in attenuation coefficients proved valuable for understanding the extent of tissue modification, guiding clinical decision-making in atrial fibrillation treatment by highlighting optimal ablation durations and identifying regions requiring further intervention.

To examine how ablation duration influences human left atrial tissue, mean attenuation coefficients within the ablation area (Fig. 5(a)) were measured across five ablation times (i.e., 20 s, 40 s, 60 s, 80 s, and 100 s) for five different hearts (Heart 1 through Heart 5) (Fig. 5). Baseline

Biomedical Optics EXPRESS

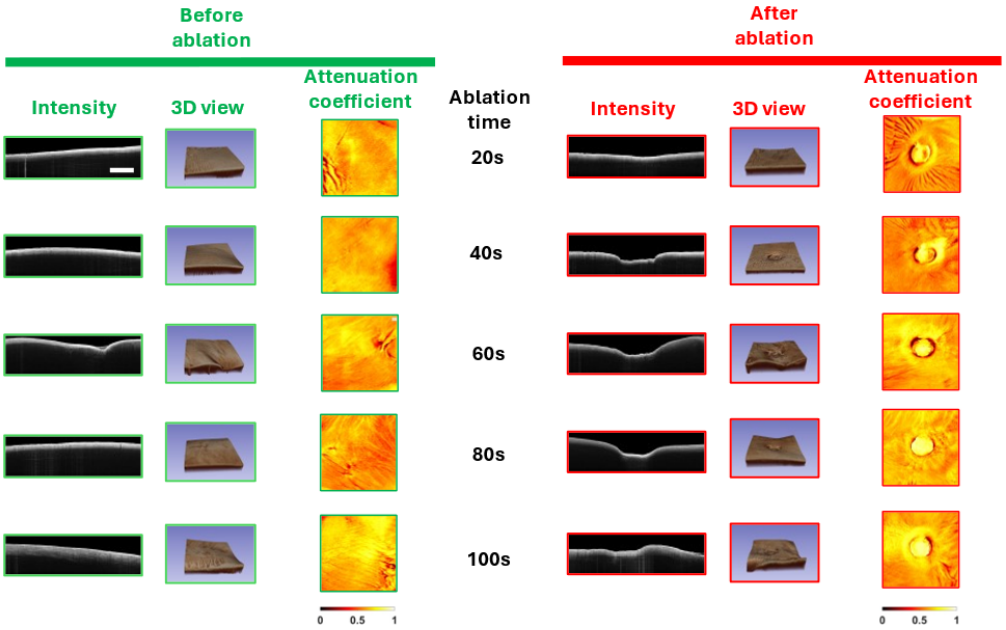

Fig. 4. SD-OCT intensity images, corresponding 3D views, and attenuation coefficient maps of human left atrium tissue before and after RF ablation at 20 s, 40 s, 60 s, 80 s, and 100 s. The dimensions of attenuation coefficient images are 9 mm x 9 mm. Scale bar: 1.2 mm.

attenuation coefficient measured before ablation (at 0) s is also plotted in Fig. 5(b). Figure 5(b) presents a line plot illustrating the mean attenuation coefficients at each ablation duration for individual hearts. Each line represents the trend of attenuation coefficient changes within the ablated region of a single heart as the ablation duration increased from 0 to 100 seconds. While a general upward trend was observed, indicating progressive tissue alteration with longer ablation, the magnitude and pattern of change varied among hearts, reflecting inter-sample variability in tissue response to thermal damage. The boxplot in Fig. 5(c) summarizes the mean attenuation coefficients across all five hearts at each ablation duration. A consistent increase in median values, indicated by the horizontal line within each box, with longer ablation durations suggests a cumulative effect of thermal injury on tissue optical properties. To investigate the effect of ablation duration on tissue attenuation, a one-way ANOVA was performed, yielding a p-value of 1.09×10^{-8}. This statistically significant result ($p < 0.05$) indicates that ablation duration has a meaningful impact on attenuation coefficients, with at least one time point showing a clear difference. These findings, supported by both visual and statistical analyses, highlight a direct relationship between ablation time and tissue alteration.

3.3. *Attenuation coefficient trends over ablation time*

Figure 6 illustrates histological evidence of ablation at 20, 40, 60, 80 and 100 seconds of ablation time in a, b, c, d and e respectively using Trichrome staining. Red dots in each panel indicate indentations on the tissue surface, which mark the ablation sites.

On top of that, Fig. 7 serves as a clear example of an ablation evidence image, showcasing reticulin fiber staining. Figure 7(a) presents a region where no ablation has occurred, displaying a more uniform and robust reticulin fiber staining, serving as a baseline for reference. In contrast, a marked reduction in staining intensity is observed within the ablated area in Fig. 7(b), where the lighter region (highlighted by arrows) likely reflects protein denaturation caused by RF energy,

Biomedical Optics EXPRESS

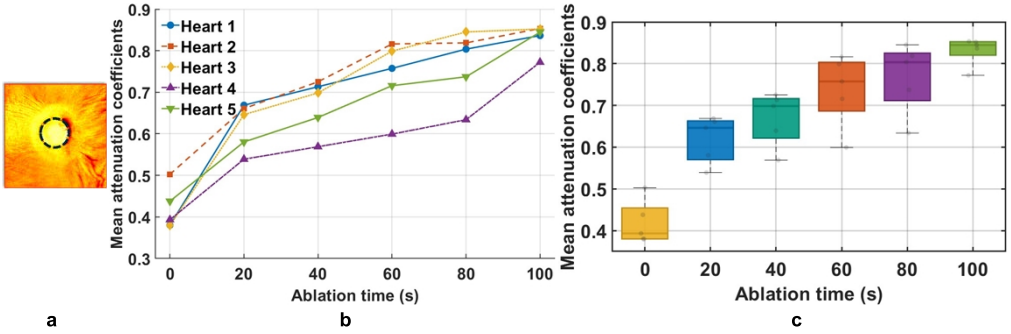

Fig. 5. Trends in attenuation coefficients with increasing ablation time. (a) Mean attenuation coefficient calculated within the ablated area (indicated by the black circle). (b) Line plot showing the mean attenuation coefficients across ablation durations for each individual heart. (c) Box plot summarizing the distribution of mean attenuation coefficients at each ablation duration, aggregated across all five hearts.

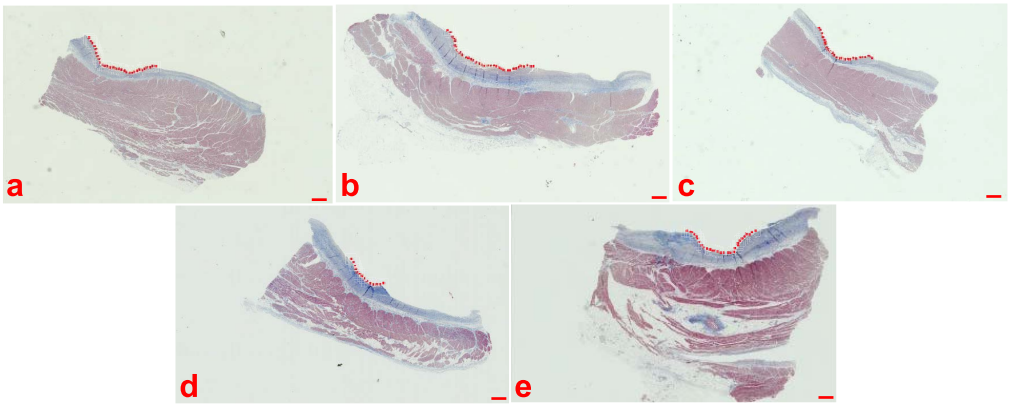

Fig. 6. Trichrome-stained tissue sections showing evidence of ablation at 20, 40, 60, 80, and 100 seconds of ablation time, corresponding to panels a–e, respectively. Red dots mark the indentation regions caused by ablation. Scale bar: 500 μm.

diminishing the tissue's ability to retain the stain compared to the surrounding non-ablated tissue. This differential staining pattern suggests that the ablation process has altered the structural integrity of the extracellular matrix, particularly the reticulin network, consistent with thermally induced tissue damage. Radiofrequency ablation (RFA) induces localized thermal coagulative necrosis, profoundly impacting the extracellular matrix (ECM) architecture. Histopathological assessment using reticulin fiber staining, which selectively visualizes argyrophilic type III collagen, demonstrates distinct differential patterns, post-RFA. In the ablated zone, the reticulin network typically exhibits fragmentation, diminished staining intensity, or complete effacement, reflecting denaturation and loss of these fine structural proteins. This contrasts with the preserved, organized reticulin framework in adjacent non ablated tissue, thereby confirming a significant alteration in ECM structural integrity directly attributable to the RFA-induced thermal ablation. This leads to a scarred region with a distinct, often denser and less organized, collagenous structure compared to the native reticulin scaffold [40–43].

4. Discussion and conclusions

This study quantitatively assessed the effects of RF ablation on human left atrial tissue using

Biomedical Optics EXPRESS

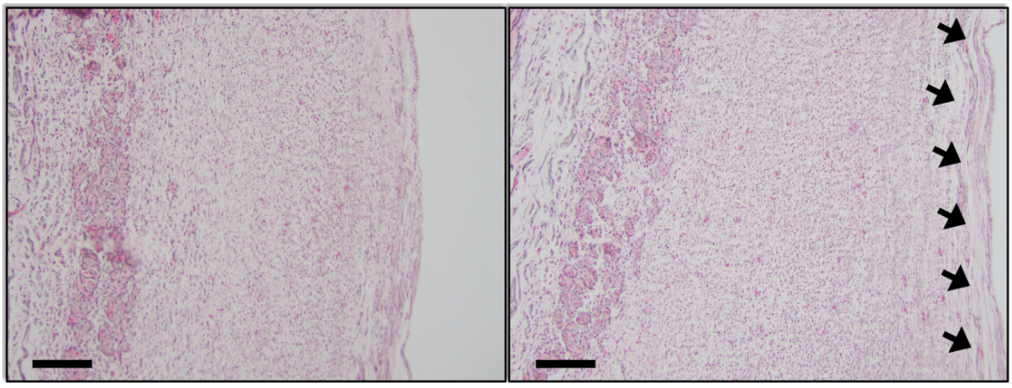

a b

Fig. 7. Reticulin fiber staining results. (a) The non-ablated region exhibits uniform and robust reticulin fiber staining. (b) The ablated region showing reduced staining intensity (indicated by arrow) due to protein denaturation and altered extracellular matrix integrity. Scale bar: 60 μm.

SD-OCT, with a particular focus on changes in attenuation coefficients as indicators of tissue alteration. Both intensity images and attenuation coefficient maps revealed progressive structural and optical changes in relation to the ablation duration (Fig. 4 and Fig. 5). While conventional OCT intensity images captured surface indentations, attenuation coefficient mapping provided a more sensitive and quantitative assessment of subsurface tissue transformation. These findings align with the known outcomes of thermal ablation, where increased RF energy delivery leads to greater cellular disruption and collagen denaturation, modifying tissue optical properties.

The ability of attenuation coefficient maps to detect subtle tissue changes prior to visible surface alterations was particularly evident at 20 seconds of ablation. The tissue surface appeared minimal changes in the OCT intensity images, whereas the attenuation map highlighted the region of increased optical attenuation, suggesting early structural alterations at the microscopic level. This indicates that attenuation-based analysis can serve as a sensitive biomarker for detecting early-stage thermal injury. By detecting subsurface changes not yet visible in conventional OCT images, attenuation mapping complements intensity imaging and provides a more detailed view of tissue alteration.

As the ablation duration increased from 40 to 100 seconds, both OCT intensity images and attenuation coefficient maps revealed more pronounced structural alterations. Surface indentations became evident in the intensity images and 3D reconstructions, while attenuation maps displayed regions of increased optical attenuation. This duration-dependent trend reflects cumulative thermal injury, consistent with collagen denaturation and cellular disruption. Quantitatively, the mean attenuation coefficients measured within the ablated regions increased consistently with ablation duration across all five heart samples (Fig. 5). Despite some inter-sample variability, the overall trend was statistically significant (ANOVA $p = 1.09 \times 10^{-8}$), indicating that ablation time has a significant effect on attenuation coefficients.

The variability observed in attenuation coefficient trends across different heart samples can be attributed to several biological factors. Age is known to affect cardiac tissue structure, with older hearts typically showing increased collagen deposition and fibrosis, which can raise optical scattering and thus the measured attenuation coefficient [44]. Differences in tissue composition, such as varying amounts of adipose tissue, fibrotic myocardium, and collagen content, also influence attenuation values, as these components have distinct optical properties and scatter light differently [45]. Additionally, underlying comorbidities and pathological changes (e.g., vascular

Biomedical Optics EXPRESS

calcifications, or prior surgeries), may further alter tissue microstructure and contribute to the observed variability.

These findings reinforce that attenuation mapping is a reliable quantitative marker of lesion development and tissue modification following RF ablation, underscoring the potential of SD-OCT as a valuable tool in monitoring lesion formation. By reflecting cumulative thermal damage, attenuation coefficients offer insights into subsurface structural changes, providing a more sensitive and objective alternative to conventional intensity-based imaging. Integrating OCT into forward-imaging catheters compatible with ablation procedures has been demonstrated in prior studies, establishing a technical foundation for real-time intraprocedural imaging [15,46–49]. Building on this, the seamless incorporation of attenuation coefficient mapping into OCT data processing pipelines, enabled by U-Net-based segmentation and automated calculation, can provide immediate, quantitative feedback on tissue alterations at the ablation site. In the clinical setting, this capability could be incorporated into existing ablation systems to offer surgeons live feedback on lesion development, allowing for dynamic adjustment of ablation duration and intensity. Such feedback would help ensure the creation of effective, transmural lesions while minimizing unnecessary tissue damage, thereby enhancing the safety, precision, and efficacy of AF ablation procedures.

While the results are promising, there are several limitations to consider in this study. The use of five fresh human hearts in this *ex vivo* study provides critical insight into lesion formation and optical property changes in left atrial tissue following RF ablation under well-controlled and replicable laboratory conditions. Nevertheless, the small sample size and inherent biological variability among donor tissues must be acknowledged as limitations that may impact the broader applicability of the results.

Besides, *ex vivo* models, while highly valuable for technique development and mechanistic investigations, cannot fully replicate the complex physiological environment of a living heart, including ongoing perfusion, neurohormonal regulation, and immune response [50,51]; *ex vivo* models are also intrinsically limited in their ability to assess long-term tissue responses such as healing, fibrous remodeling, and potential arrhythmogenicity following ablation—critical endpoints for determining optimal ablation strategies and clinical efficacy [52,53]. Despite these constraints, a recent study [54] has demonstrated that carefully optimized *ex vivo* protocols can produce ablation lesions with characteristics closely resembling those seen in validated *in vivo* or clinical models, thereby providing a reliable platform for comparative testing of catheters and energy delivery protocols while also reducing the need for animal or human *in vivo* studies. Our assessment therefore focuses on the immediate morphological and optical effects post-ablation.

Additionally, due to the limited availability of atrial OCT data, the U-Net was trained on liver OCT images rather than cardiac tissue. We acknowledge that models trained solely on liver OCT images might experience domain shift effects when directly applied to segment heart images, a common challenge in medical imaging due to limited labeled data. In this study, we found that even a lightweight U-Net model, despite being trained on liver data, demonstrated robust performance in the cardiac segmentation task. This suggests a degree of task resemblance or sufficient feature overlap: delineating tissue regions from above empty background, which may reduce the demand on the model's generalization capability. The current approach, training on liver OCT data and using the model on heart OCT image segmentation, reflects a practical and flexible cross-domain solution. Although tissue types differ, the structural similarity of the object mitigates the challenge brought about by domain shift and facilitates model transferability.

In vivo studies and clinical trials have established that lesion maturation and atrial structural changes can continue for months after ablation, affecting long-term rhythm outcomes and the risk of recurrence or complications [55]. Future research incorporating chronic animal models or longitudinal clinical follow-up will be needed to bridge the gap between acute observations made in *ex vivo* systems and real-world clinical outcomes, including guidance on optimal ablation

Biomedical Optics EXPRESS

parameters and complication management. In future work, we will explore labeling additional heart OCT images for fine-tuning, aiming to further improve segmentation performance and mitigate domain shift effects. Moreover, integrating complementary imaging modalities, such as polarization-sensitive OCT, could offer additional insights into post-ablation birefringence changes, further enhancing our understanding of thermal injury effects.

Funding. National Institutes of Health (R01DK133717, P20 GM135009, P20GM103639, P30CA225520); National Science Foundation (OIA-2132161, 2238648); Oklahoma Center for the Advancement of Science and Technology (HR23-071); University of Oklahoma Norman Campus (Data Institute for Societal Challenges, the Research Council, Libraries' Open Access Fund).

Acknowledgement. This work was supported by grants from the University of Oklahoma Health Sciences Center (P30CA225520), National Science Foundation (OIA-2132161, 2238648), National Institutes of Health (R01DK133717), Oklahoma Center for the Advancement of Science and Technology (HR23-071), the medical imaging COBRE (P20 GM135009), the Prevent Cancer Foundation, and a grant from the Data Institute for Societal Challenges and the Research Council funded by the Office of the Vice President for Research and Partnerships of the University of Oklahoma Norman Campus. Histology service provided by the Tissue Pathology Shared Resource was supported in part by the National Institute of General Medical Sciences COBRE Grant P20GM103639 and National Cancer Institute Grant P30CA225520 of the National Institutes of Health. Financial support was provided by the OU Libraries' Open Access Fund.

Disclosures. The authors declare no competing interests

Data availability. Data underlying the results presented in this paper are not publicly available at this time but may be obtained from the authors upon reasonable request.

Supplemental document. See Supplement 1 for supporting content.

References

1. E. J. Benjamin, P. A. Wolf, R. B. D'Agostino, *et al.*, "Impact of atrial fibrillation on the risk of death: the Framingham Heart Study," Circulation **98**(10), 946–952 (1998).
2. P. Kirchhof and S. Benussi, "2016 ESC Guidelines for the management of atrial fibrillation developed in collaboration with EACTS," Eur. Heart J. **37**(38), 2893–2962 (2016).
3. M. Haissaguerre and P. Jaïs, "Spontaneous initiation of atrial fibrillation by ectopic beats originating in the pulmonary veins," N. Engl. J. Med. **339**(10), 659–666 (1998).
4. H. Calkins, G. Hindricks, R. Cappato, *et al.*, "2017 HRS/EHRA/ECAS/APHRS/SOLAECE expert consensus statement on catheter and surgical ablation of atrial," Heart Rhythm **14**(10), e275–e444 (2017).
5. R. Cappato, H. Calkins, S.-.A Chen, *et al.*, "Worldwide survey on the methods, efficacy, and safety of catheter ablation for human atrial fibrillation," Circulation **111**(9), 1100–1105 (2005).
6. D. Shah, "A critical appraisal of cardiac ablation technology for catheter-based treatment of atrial fibrillation," Expert Rev. Med. Devices **8**(1), 49–55 (2011).
7. A. Natale, V. Y. Reddy, G. Monir, *et al.*, "Paroxysmal AF catheter ablation with a contact force sensing catheter: results of the prospective, multicenter SMART-AF trial," J. Am. Coll. Cardiol. **64**(7), 647–656 (2014).
8. A. Bulava, J. Haniš, D. Sitek, *et al.*, "Catheter ablation for paroxysmal atrial fibrillation: a randomized comparison between multielectrode catheter and point-by-point ablation," Pacing and Clinical Electrophysiology **33**(9), 1039–1046 (2010).
9. S. Y. Ho, D. Sanchez-Quintana, J. A. Cabrera, *et al.*, "Anatomy of the left atrium: implications for radiofrequency ablation of atrial fibrillation," J. Cardiovasc. Electrophysiol. **10**(11), 1525–1533 (1999).
10. D. Sánchez-Quintana, J. A. Cabrera, V. Climent, *et al.*, "Anatomic relations between the esophagus and left atrium and relevance for ablation of atrial fibrillation," Circulation **112**(10), 1400–1405 (2005).
11. T. Arentz, L. Macle, D. Kalusche, *et al.*, ""Dormant" pulmonary vein conduction revealed by adenosine after ostial radiofrequency catheter ablation," J. Cardiovasc. Electrophysiol. **15**(9), 1041–1047 (2004).
12. G. J. Tearney, M. E. Brezinski, B. E. Bouma, *et al.*, "In vivo endoscopic optical biopsy with optical coherence tomography," Science **276**(5321), 2037–2039 (1997).
13. R. P. Singh-Moon, C. C. Marboe, and C. P. Hendon, "Near-infrared spectroscopy integrated catheter for characterization of myocardial tissues: preliminary demonstrations to radiofrequency ablation therapy for atrial fibrillation," Biomed. Opt. Express **6**(7), 2494–2511 (2015).
14. D. Liang, D. Taeschler, C. Goepfert, *et al.*, "Radiofrequency ablation lesion assessment using optical coherence tomography–a proof-of-concept study," J. Cardiovasc. Electrophysiol. **30**(6), 934–940 (2019).
15. H. Wang, W. Kang, A. P. Bishop, *et al.*, "In vivo intracardiac optical coherence tomography imaging through percutaneous access: toward image-guided radio-frequency ablation," J. Biomed. Opt. **16**(11), 1 (2011).
16. O. Ronneberger, P. Fischer, and T. Brox, "U-net: Convolutional networks for biomedical image segmentation," in *Medical image computing and computer-assisted intervention–MICCAI 2015: 18th international conference, Munich, Germany, October 5-9, 2015, proceedings, part III 18*, 2015: Springer, pp. 234–241.
17. K. Zhang, W. Zuo, Y. Chen, *et al.*, "Beyond a gaussian denoiser: Residual learning of deep cnn for image denoising," IEEE Trans. on Image Process. **26**(7), 3142–3155 (2017).

Biomedical Optics EXPRESS

18. J. Dewire and H. Calkins, "Update on atrial fibrillation catheter ablation technologies and techniques," Nat. Rev. Cardiol. **10**(10), 599–612 (2013).
19. D. L. Packer, D. B. Mark, R. A. Robb, *et al.*, "Effect of catheter ablation vs antiarrhythmic drug therapy on mortality, stroke, bleeding, and cardiac arrest among patients with atrial fibrillation: the CABANA randomized clinical trial," Jama **321**(13), 1261–1274 (2019).
20. T. J. Badger, M. Daccarett, N. W. Akoum, *et al.*, "Evaluation of left atrial lesions after initial and repeat atrial fibrillation ablation: lessons learned from delayed-enhancement MRI in repeat ablation procedures," Circ.: Arrhythmia Electrophysiol. **3**(3), 249–259 (2010).
21. G. R. Vergara, S. Vijayakumar, E. G. Kholmovski, *et al.*, "Real-time magnetic resonance imaging–guided radiofrequency atrial ablation and visualization of lesion formation at 3 Tesla," Heart Rhythm **8**(2), 295–303 (2011).
22. H. Yang, J. A. Majumder, Z. Huang, *et al.*, "Robust, high-density lesion mapping in the left atrium with near-infrared spectroscopy," J. Biomed. Opt. **29**(02), 028001 (2024).
23. X. Yu, R. P. Singh-Moon, and C. P. Hendon, "Real-time assessment of catheter contact and orientation using an integrated optical coherence tomography cardiac ablation catheter," Appl. Opt. **58**(14), 3823–3829 (2019).
24. K. Garrott, J. Laughner, S. Gutbrod, *et al.*, "Combined local impedance and contact force for radiofrequency ablation assessment," Heart rhythm **17**(8), 1371–1380 (2020).
25. C. A. Martin, R. Martin, P. R. Gajendragadkar, *et al.*, "First clinical use of novel ablation catheter incorporating local impedance data," J. Cardiovasc. Electrophysiol. **29**(9), 1197–1206 (2018).
26. S. Conti, A. Verma, A. Natale, *et al.*, "Atrial fibrillation: insights on mechanisms, mapping and catheter ablation," vol. 10, ed: Frontiers Media SA, 2023, p. 1280925.
27. Y. Huo, T. Gaspar, Y. Schönbauer, *et al.*, "Low-voltage myocardium-guided ablation trial of persistent atrial fibrillation," NEJM Evidence **1**(11), 2200141 (2022).
28. J. M. Lee, Sang Won Kim, C. A. Li, *et al.*, "Saline-enhanced radiofrequency thermal ablation of the lung: a feasibility study in rabbits," Korean J. Radiol. **3**(4), 245–253 (2002).
29. K.-M. Fung, J. H. Chakrabarty, W. F. Kern, *et al.*, "Intravascular large B-cell lymphoma with hemophagocytic syndrome (Asian variant) in a Caucasian patient," International Journal of Clinical and Experimental Pathology **5**(5), 448 (2012).
30. P. Isola, J.-Y. Zhu, T. Zhou, *et al.*, "Image-to-image translation with conditional adversarial networks," in *Proceedings of the IEEE conference on computer vision and pattern recognition*, 2017, pp. 1125–1134.
31. X. Xiong, Z. Wu, S. Tan, *et al.*, "Sam2-unet: Segment anything 2 makes strong encoder for natural and medical image segmentation," arXiv (2024).
32. K. He, X. Zhang, S. Ren, *et al.*, "Deep residual learning for image recognition," in *Proceedings of the IEEE conference on computer vision and pattern recognition*, 2016, pp. 770–778.
33. F. Isensee, P. F. Jaeger, S. A. Kohl, *et al.*, "nnU-Net: a self-configuring method for deep learning-based biomedical image segmentation," Nat. Methods **18**(2), 203–211 (2021).
34. Z. Wu, J.-Y. Yang, C.-B. Yan, *et al.*, "Integrating SAM priors with U-Net for enhanced multiclass cell detection in digital pathology," Sci. Rep. **15**(1), 15641 (2025).
35. F. Yan, Q. Zhang, B. M. Mutembei, *et al.*, "Comprehensive Evaluation of Human Donor Liver Viability with Polarization-Sensitive Optical Coherence Tomography," medRxiv (2025).
36. C. Wang, H. Cui, Q. Zhang, *et al.*, "Automatic renal carcinoma biopsy guidance using forward-viewing endoscopic optical coherence tomography and deep learning," Commun. Eng. **3**(1), 107 (2024).
37. D. P. Huttenlocher, G. A. Klanderman, and W. J. Rucklidge, "Comparing images using the Hausdorff distance," IEEE Trans. Pattern Anal. Machine Intell. **15**(9), 850–863 (1993).
38. A. A. Taha and A. Hanbury, "Metrics for evaluating 3D medical image segmentation: analysis, selection, and tool," BMC Med. Imaging **15**(1), 29 (2015).
39. N. Ravi, V. Gabeur, Y.-T. Hu, *et al.*, "Sam 2: Segment anything in images and videos," arXiv (2024).
40. N. Trofimov, A. Rodionov, D. Egorov, *et al.*, "Histological Justification for the Need of Radiofrequency Ablation of Pulmonary Arteries in Patients with High-Grade Secondary Pulmonary Hypertension," Sovrem Tekhnologii Med. **13**(6), 56–62 (2021).
41. F. Collettini, C. Reimann, J. Brangsch, *et al.*, "Elastin-specific MRI of extracellular matrix-remodelling following hepatic radiofrequency-ablation in a VX2 liver tumor model," Sci. Rep. **11**(1), 6814 (2021).
42. B. D. Zelickson, D. Kist, E. Bernstein, *et al.*, "Histological and ultrastructural evaluation of the effects of a radiofrequency-based nonablative dermal remodeling device: a pilot study," Arch. Dermatol. **140**(2), 204–209 (2004).
43. H. U. Kasper, C. Bangard, A. Gossmann, *et al.*, "Pathomorphological changes after radiofrequency ablation in the liver," Pathol. Int. **60**(3), 149–155 (2010).
44. J. M. Bueno, R. M. Martínez-Ojeda, M. Pérez-Zabalza, *et al.*, "Analysis of age-related changes in the left ventricular myocardium with multiphoton microscopy," Biomed. Opt. Express **15**(5), 3251–3264 (2024).
45. Y. Gan, T. H. Lye, C. C. Marboe, *et al.*, "Characterization of the human myocardium by optical coherence tomography," J. Biophotonics **12**(12), e201900094 (2019).
46. C. P. Fleming, H. Wang, K. J. Quan, *et al.*, "Real-time monitoring of cardiac radio-frequency ablation lesion formation using an optical coherence tomography forward-imaging catheter," J. Biomed. Opt. **15**(03), 1–030516 (2010).

Biomedical Optics EXPRESS

47. C. P. Fleming, K. J. Quan, H. Wang, *et al.*, "In vitro characterization of cardiac radiofrequency ablation lesions using optical coherence tomography," Opt. Express **18**(3), 3079–3092 (2010).
48. R. P. Martins, G. Papiashvili, A. Sabirov, *et al.*, "First-in-human trial of atrial fibrillation ablation using real-time tissue optical assessment to predict pulsed field lesion durability," Europace **27**(2), euaf009 (2025).
49. Z. Huang, X. Zhao, O. Ziv, *et al.*, "Automated analysis framework for in vivo cardiac ablation therapy monitoring with optical coherence tomography," Biomed. Opt. Express **14**(3), 1228–1242 (2023).
50. L. Shahgholi, N. Ortiz, T. Naeimi, *et al.*, "Adipose tissue impacts radiofrequency ablation lesion size: results of an ex vivo poultry model," Pain Physician **26**(7), 569–574 (2023).
51. C. S. Lacko, Q. Chen, V. Mendoza, *et al.*, "Development of a clinically relevant ex vivo model of cardiac ablation for testing of ablation catheters," J. Cardiovasc. Electrophysiol. **34**(3), 682–692 (2023).
52. A. W. Teh, P. M. Kistler, G. Lee, *et al.*, "Long-term effects of catheter ablation for lone atrial fibrillation: progressive atrial electroanatomic substrate remodeling despite successful ablation," Heart Rhythm **9**(4), 473–480 (2012).
53. L. You, L. Yao, B. Zhou, *et al.*, "Effects of different ablation strategies on long-term left atrial function in patients with paroxysmal atrial fibrillation: a single-blind randomized controlled trial," Sci. Rep. **9**(1), 7695 (2019).
54. H. Nakagawa, S. Farshchi-Heydari, J. Maffre, *et al.*, "Evaluation of ablation parameters to predict irreversible lesion size during pulsed field ablation," Circ.: Arrhythmia Electrophysiol. **17**(8), e012814 (2024).
55. N. Erhard, F. Bahlke, B. Neuner, *et al.*, "Early ablation leads to better outcome in patients< 55 years with persistent atrial fibrillation," Sci. Rep. **14**(1), 25370 (2024).